# Vascular $K_{ATP}$ channel structural dynamics reveal regulatory mechanism by Mg-nucleotides

Min Woo Sung[a], Zhongying Yang[a], Camden M. Driggers[a], Bruce L. Patton[a], Barmak Mostofian[b], John D. Russo[b], Daniel M. Zuckerman[b], and Show-Ling Shyng[a,1]

[a]Department of Chemical Physiology and Biochemistry, School of Medicine, Oregon Health and Science University, Portland, OR 97239; and [b]Department of Biomedical Engineering, School of Medicine, Oregon Health and Science University, Portland, OR 97239

Edited by Nieng Yan, Princeton University, Princeton, NJ, and approved August 30, 2021 (received for review May 21, 2021)

**Vascular tone is dependent on smooth muscle $K_{ATP}$ channels comprising pore-forming Kir6.1 and regulatory SUR2B subunits, in which mutations cause Cantú syndrome. Unique among $K_{ATP}$ isoforms, they lack spontaneous activity and require Mg-nucleotides for activation. Structural mechanisms underlying these properties are unknown. Here, we determined cryogenic electron microscopy structures of vascular $K_{ATP}$ channels bound to inhibitory ATP and glibenclamide, which differ informatively from similarly determined pancreatic $K_{ATP}$ channel isoform (Kir6.2/SUR1). Unlike SUR1, SUR2B subunits adopt distinct rotational "propeller" and "quatrefoil" geometries surrounding their Kir6.1 core. The glutamate/aspartate-rich linker connecting the two halves of the SUR-ABC core is observed in a quatrefoil-like conformation. Molecular dynamics simulations reveal MgADP-dependent dynamic tripartite interactions between this linker, SUR2B, and Kir6.1. The structures captured implicate a progression of intermediate states between MgADP-free inactivated, and MgADP-bound activated conformations wherein the glutamate/aspartate-rich linker participates as mobile autoinhibitory domain, suggesting a conformational pathway toward $K_{ATP}$ channel activation.**

ATP-sensitive potassium channel | sulfonylurea receptor 2B | Kir6.1 | Cantú syndrome | ABC transporter

Dynamic regulation of $K^+$ channel gating is a primary point of control for processes governed by electrical excitability. ATP-sensitive potassium ($K_{ATP}$) channels, regulated by intracellular ATP to ADP ratios, transduce metabolic changes into electrical signals to govern many physiological processes (1). They are uniquely evolved hetero-octameric complexes comprising four pore-forming inwardly rectifying potassium channel subunits, Kir6.x, and four regulatory sulfonylurea receptors, SURx, nontransporting members of the ABCC subfamily of ABC transporters (2). Various Kir6.x/SURx combinations generate channel isoforms with distinct tissue distribution and function (3, 4). Kir6.2/SUR1 channels are expressed in pancreatic β cells and control glucose-stimulated insulin secretion. Kir6.2/SUR2A channels are the predominant isoform in myocardium, while Kir6.1/SUR2B channels are the major isoform found in vascular smooth muscle. SUR2A and 2B are two splice variants of *ABCC9* that differ in their C-terminal 42 amino acids (aa). In vascular smooth muscle, $K_{ATP}$ activation leads to membrane hyperpolarization and vasodilation (5), while inhibition or deletion causes membrane depolarization, vasoconstriction, and hypertension (5–8). Mutations in the vascular $K_{ATP}$ channel genes (*KCNJ8* and *ABCC9*) cause Cantú syndrome (9–11), a severe pleiotropic systemic hypotension disorder including hypertrichosis, osteochondrodysplasia, and cardiomegaly (12).

$K_{ATP}$ channel gating by intracellular ATP and ADP involves allosteric sites on both subunits. ATP binding to Kir6.x inhibits the channel. SURx, through induced dimerization of the paired nucleotide binding domains (NBDs), requiring MgADP bound to NBD2 and MgATP bound to noncatalytic NBD1, activates the channel (1, 4, 13). Like all Kir channels, opening further requires $PIP_2$ bound to Kir6.x (14–16). Despite these commonalities, vascular Kir6.1/SUR2B $K_{ATP}$ channels have distinct biophysical properties, nucleotide sensitivities, and pharmacology that differentiate them from other isoforms (17–19). First, vascular $K_{ATP}$ channel unitary conductance is half that of Kir6.2-containing channels. Second, vascular channels lack spontaneous activity, only opening in the presence of NBD-dimerizing Mg-dinucleotides/trinucleotides; in contrast, pancreatic or cardiac channels containing Kir6.2 open spontaneously in the absence of ATP. Third, once activated, vascular $K_{ATP}$ channels are relatively insensitive to ATP inhibition, requiring mM concentrations to observe an effect, while their pancreatic or cardiac counterparts are blocked by ATP at μM concentrations. Lastly, the antidiabetic sulfonylurea drug glibenclamide (Glib), which inhibits SUR1-containing pancreatic channels with high affinity, is ∼10-fold less potent toward the vascular and cardiac channels containing SUR2. Glib has been shown to reverse defects from gain-of-function Cantú mutations in mice (20). However, clinical application in Cantú patients is hindered by hypoglycemia from inhibition of pancreatic channels (21). Structural mechanisms underlying unique biophysical, physiological, and pharmacological properties among $K_{ATP}$ channels are unknown.

Here, we report cryogenic electron microscopy (cryoEM) structures for the vascular $K_{ATP}$ channel, Kir6.1/SUR2B, in the presence of ATP and Glib. The structures show conformations not previously seen in pancreatic $K_{ATP}$ channels prepared under the

## Significance

**Vascular $K_{ATP}$ channels formed by the potassium channel Kir6.1 and its regulatory protein SUR2B maintain blood pressure in the physiological range. Overactivity of the channel due to genetic mutations in either Kir6.1 or SUR2B causes severe cardiovascular pathologies known as Cantú syndrome. The cryogenic electron microscopy structures of the vascular $K_{ATP}$ channel reported here show multiple, dynamically related conformations of the regulatory subunit SUR2B. Molecular dynamics simulations reveal the negatively charged ED-domain in SUR2B, a stretch of 15 glutamate (E) and aspartate (D) residues not previously resolved, play a key MgADP-dependent role in mediating interactions at the interface between the SUR2B and Kir6.1 subunits. Our findings provide a mechanistic understanding of how channel activity is regulated by intracellular MgADP.**

Author contributions: M.W.S., D.M.Z., and S.-L.S. designed research; M.W.S., Z.Y., C.M.D., B.M., J.D.R., and S.-L.S. performed research; M.W.S., C.M.D., B.M., J.D.R., and S.-L.S. analyzed data; and M.W.S., B.L.P., D.M.Z., and S.-L.S. wrote the paper.

The authors declare no competing interest.

This article is a PNAS Direct Submission.

[1]To whom correspondence may be addressed. Email: shyngs@ohsu.edu.

This article contains supporting information online at http://www.pnas.org/lookup/suppl/doi:10.1073/pnas.2109441118/-/DCSupplemental.

same condition (22–24). First, unlike in Kir6.2, Kir6.1 cytoplasmic domains (CDs) were displaced from the membrane too far to interact with $PIP_2$ for channel opening. Second, unlike pancreatic channels, which have a predominant propeller-shaped conformation when bound to ATP and Glib (22, 24), vascular $K_{ATP}$ channels held four distinct conformations, two resembling propellers and two quatrefoils, marked by varying degrees of rotation of SUR2B toward the core Kir6.1 tetramer. Importantly, a long segment of SUR not previously resolved in any $K_{ATP}$ structures, linking NBD1 and transmembrane domain 2 (TMD2), was revealed within vascular $K_{ATP}$ structures to mediate the cytosolic interface between SUR2B and Kir6.1. In particular, the linker's unique 15 glutamate/aspartate residues termed the ED-domain (25) established a nexus of interactions engaging SUR2B-NBD2 with Kir6.1 C-terminal domain (CTD). Molecular dynamics (MD) simulations showed MgADP binding to NBD2 was accompanied by substantial reconfiguration at this nexus, revealing the ED-domain provides a mobile autoinhibitory interaction that guards the transition of SUR2B from MgADP-free inactivated state to MgADP-bound activated state. Together, our findings point to a structural pathway through which SUR regulates Kir6 channel gating.

## Results and Discussion

**Structure Determination of Kir6.1/SUR2B $K_{ATP}$ Channels with ATP and Glib.** Vascular $K_{ATP}$ channels were purified from COSm6 cells coexpressing rat Kir6.1 and SUR2B (97.6 and 97.2% sequence identity to human Kir6.1 and SUR2B, respectively). COSm6 cells lack endogenous $K_{ATP}$ channels and have been used extensively as a heterologous expression system for $K_{ATP}$ channel structure–function studies (16, 26). Channels were solubilized in digitonin, purified via an SUR2B epitope tag, and imaged in the presence of 1 mM ATP (no $Mg^{2+}$) and 10 μM Glib on graphene oxide–coated grids, as described in *Materials and Methods*.

In vascular $K_{ATP}$ channel structures as in pancreatic channels, we found SUR2B anchored to Kir6.1 via interactions mediated by transmembrane helix 1 (TM1) of SUR2B-TMD0 and Kir6.1-TM1 (Fig. 1). However, conformational deviations from fourfold symmetry of the SUR2B were noted in two-dimensional class averages (*SI Appendix*, Fig. S1). To obtain clear SUR2B maps, we implemented symmetry expansion and extensive focused three-dimensional (3D) classification of Kir6.1 tetramer with individual SUR2B (*Materials and Methods*) (*SI Appendix*, Fig. S2), which isolated four 3D classes having identical Kir6.1 tetramer structures but different SUR2B orientations (Fig. 1 and *SI Appendix*, Fig. S2). When symmetrized, two of the 3D classes, designated P1 and P2, resembled the pancreatic channel propeller conformations previously reported (22, 24). The other two, designated Q1 and Q2, resembled the "quatrefoil conformation" reported for human pancreatic $K_{ATP}$ in which the SUR1 NBDs are dimerized (27). Further refinement yielded cryoEM maps with overall resolutions of 3.4, 4.2, 4.0, and 4.2 Å for the P1, P2, Q1, and Q2 conformations, respectively (*SI Appendix*, Fig. S3). The maps were sufficient to build a full atomic model for all of Kir6.1 minus the disordered C terminus (365 to 424) for all

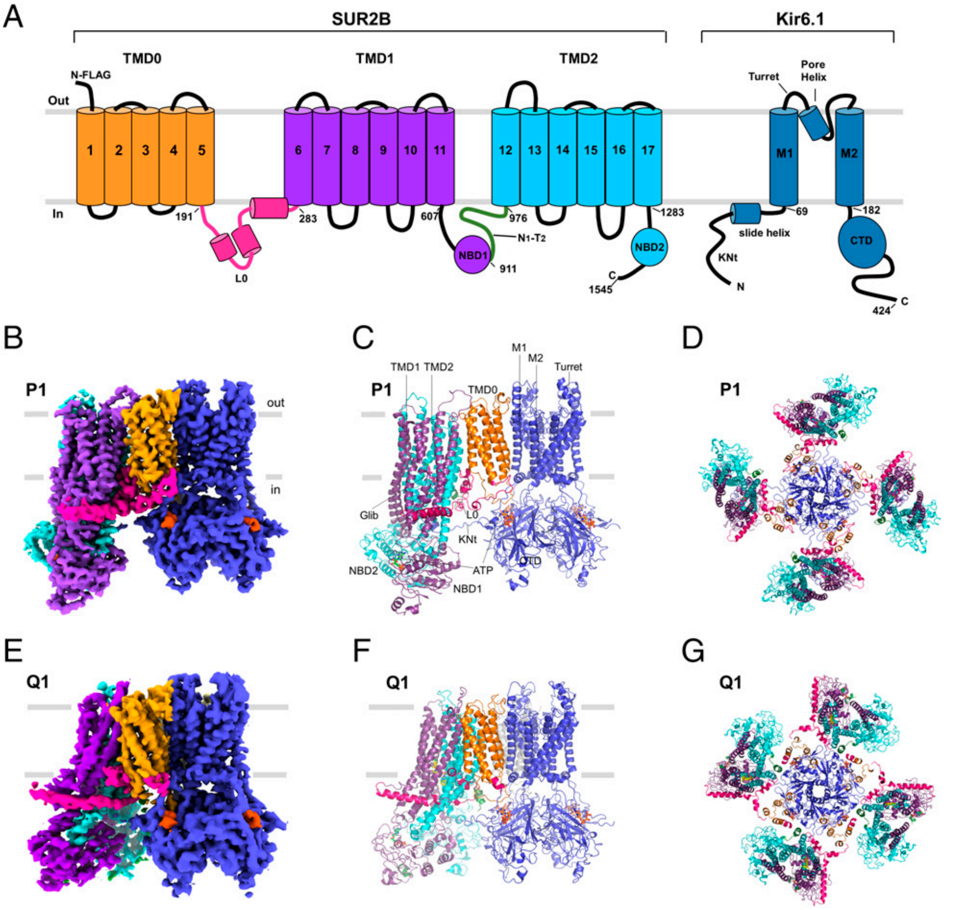

Fig. 1. Structures of the vascular $K_{ATP}$ channel in the presence of ATP and Glib. (*A*) Schematics of SUR2B and Kir6.1 domain organization. (*B*) CryoEM density map of $(Kir6.1)_4SUR2B$ P1, side view. (*C*) Structural model of $(Kir6.1)_4SUR2B$ P1, side view. (*D*) Fourfold symmetrized structure model of P1 viewed from the top (i.e., extracellular side). (*E*) CryoEM density map of $(Kir6.1)_4SUR2B$ Q1, side view. (*F*) Structural model of $(Kir6.1)_4SUR2B$ Q1, side view. (*G*) Fourfold symmetrized structure model of Q1 viewed from the top.

conformations, with clear sidechain densities for most residues (*SI Appendix*, Fig. S3*d*) and also models for most of SUR2B (see *Materials and Methods* for details). Densities for ATP, Glib, and some lipids were well resolved (*SI Appendix*, Fig. S3*d*). Significantly, the Q1 conformation included definitive densities in SUR2B for L0, which is the linker connecting TMD0 and the ABC core, and also the N1-T2 linker, which connects NBD1 to TMD2; neither is resolved in the human pancreatic $K_{ATP}$ quatrefoil structure previously determined (27). The P- and Q-like conformations differ by a major rotation of the SUR2B-ABC core toward the Kir6.1 tetramer, clockwise when viewed from the extracellular side (Fig. 1 *D* and *G*). P1 and Q1 were the dominant particle populations within the P- and Q-like forms, respectively, differing from P2 and Q2 by degree of rotation and specific features. We first focus on structural differences between P1 and Q1, which provided the highest resolutions.

**Structural Correlates of Kir6.1 Functional Divergence.** Although the Kir6.1 tetramer was similarly configured in all P and Q conformations for SUR2B, it included several features distinct from Kir6.2 in our published pancreatic channel structure determined under similar conditions with ATP and Glib (Protein Data Bank [PDB]: 6BAA). The Kir6.1 channel CD was extended intracellularly away from the membrane by ∼5.8 Å, and simultaneously counterclockwise rotated (viewed from the extracellular face) by 12.4° (Fig. 2*A*). The Kir6.x CD is thus corkscrewed away from the membrane in Kir6.1/SUR2B, compared to Kir6.2/SUR1. Constrictions in the two cytoplasmic gates, namely the helix bundle crossing (F178) and the G-loop (G304, I305), indicate a closed Kir6.1 channel pore, similar to Kir6.2 under the same condition (*SI Appendix*, Fig. S4). However, the distance between the helix bundle crossing gate and the G-loop gate is significantly larger in Kir6.1 due to the untethered CD.

In $K^+$ channels, variations in the turret region surrounding the pore entryway have been shown to affect selectivity filter stability and ion conduction (28). Compared to Kir6.2, the turret of Kir6.1 contains an extra 11 aa ($^{102}$YAYMEKGITEK$^{112}$). We found this sequence formed a helix and loop structure that extends the turret further out into the extracellular space (Fig. 2 *B* and *C*). Functional studies using Kir6.1–Kir6.2 chimeras previously identified residues in Kir6.1 thought to impart its smaller unitary conductance, specifically M148 and N123-V124-R125 (29). M148 in Kir6.1 (replacing Kir6.2-V138) was proposed to reduce pore entrance diameter, while N123 in Kir6.1 (replacing Kir6.2-S113) was hypothesized to impact an intersubunit salt bridge between R146 and E150, which in other Kir channels is formed by corresponding residues and critical for channel conduction (29, 30). However, our structure found M148 facing the pore helix (Fig. 2*C*) rather than the entrance and that no significant difference exists in the adjacent pore diameters between Kir6.1 and Kir6.2, nor in their intersubunit salt bridges. Interestingly, N123-V124-R125 of Kir6.1 is located

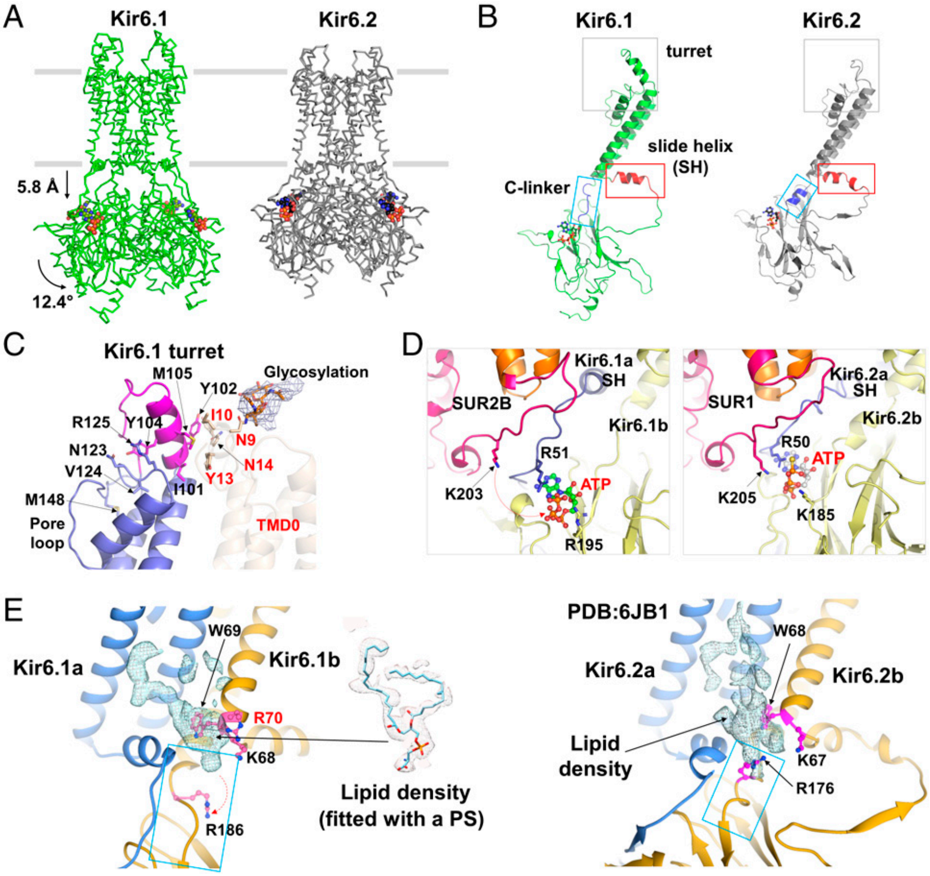

**Fig. 2.** Structural comparison between Kir6.1 and Kir6.2. (*A*) Comparison of Kir6.1 and Kir6.2 showing translational and rotational differences in the CD. (*B*) Major structural differences in the turret (gray box), SH (red box), and C-linker (cyan box) between Kir6.1 and Kir6.2. (*C*) Close-up view of the turret showing insertion of an additional 11 aa (magenta) in Kir6.1, which appears to be in position to interact with TMD0 of SUR2B (residues labeled in red). The density corresponding to glycosylation of N9 is fitted with two N-acetylglucosamines. (*D*) Close-up view of the Kir6.1 ATP binding site in comparison to Kir6.2 ATP binding site. (*E*) Close-up view of the $PIP_2$ binding site in Kir6.1 in comparison to that in Kir6.2. R70 (P69 in Kir6.2), which could interact with negatively charged phospholipid, is highlighted in red label.

between the turret extension and the pore loop and interacts with Y104 in the turret extension (Fig. 2*C*). Future mutagenesis studies will determine the contributions of these interactions to Kir6.1 channel conductance.

We next assessed structural differences between Kir6.1 and Kir6.2 in two elements intimately associated with activity at ATP and $PIP_2$ binding sites: the N-terminal amphipathic helix known as the slide helix (SH), and the connecting strand between TM2 and the CTD called the C-linker (Fig. 2 *B*, *D*, and *E*). In our Kir6.2 structure (22), SH is bent halfway at the D58 position resembling a $3_{10}$ helix (31). In contrast, SH in Kir6.1 formed a continuous helix extending toward the neighboring Kir6.1, thus compressing the $PIP_2$ binding pocket. In Kir6.2, the C-linker forms a helix that tethers the CTD close to the membrane, which positions critical $PIP_2$-binding residues such as R176 for $PIP_2$ interaction. Rather different, the C-linker in Kir6.1 unwound into an unstructured loop stretching toward the cytoplasm, which deflected R186 (corresponding to Kir6.2-R176) away from the $PIP_2$ binding site (Fig. 2 *B* and *E*). A previous study by Quinne et al. has shown that Kir6.1 binds and is modulated by $PIP_2$ (32). In our structure, we observed a strong nonprotein cryoEM density in the $PIP_2$ binding pocket. However, this density is better fitted with a phosphatidylserine (PS) than a $PIP_2$ (Fig. 2*E*). Recent MD simulations of Kir2.2 in membranes containing mixed phospholipids showed that PS can also occupy the $PIP_2$ pocket (33). Because no exogenous $PIP_2$ was added to our protein sample, the simplest interpretation of the structural data is that the more abundant PS resides in the Kir6.1 $PIP_2$ binding pocket. However, a possibility remains that the density includes endogenous $PIP_2$ or other phospholipids copurified with the channel. CryoEM densities matching ATP were clearly resolved in Kir6.1 tetramers, at sites located between the N-terminal domains and CTDs of adjacent Kir6.1 subunits, matching sites in Kir6.2/SUR1 channels. However, unlike for Kir6.2, ATP had fewer close residue interactions in Kir6.1 due to displacement of the Kir6.1-CD. In particular in pancreatic channels, SUR1-K205 (in L0) directly participates in binding ATP at its inhibitory site (23, 27, 34), while the corresponding vascular channel residue SUR2B-K203 was displaced from potential ATP binding (Fig. 2*D*). Thus, the constellation of ATP interactions was sparser and hence likely weaker when Kir6.1-CD was displaced from the membrane.

Taken together, the translocation of the Kir6.1-CD away from the membrane compromised binding of both ATP and $PIP_2$. This correlates well with the basal inactivity and reduced ATP sensitivity of the vascular $K_{ATP}$ channel compared to Kir6.2 channels (35, 36). Rotation and downward movement of the Kir6.2-CD have been detected in minor subclasses of ATP- and Glib-bound pancreatic Kir6.2/SUR1 structures (23, 24), indicating similar dynamics occur but less stably persist. Moreover, translation and/or rotation of the CD is observed in Kir2, Kir3, and bacterial Kir channels (37–40), and recent cryoEM studies of Kir3 channels found that increased $PIP_2$ concentrations shift particle distributions toward those having CD tethered close to the $PIP_2$ membrane sites (41). Thus, a common model of $K_{ATP}$ channel activity involves channel opening dependent on $PIP_2$ binding, which in turn depends on engagement by the Kir6.x-CD modulated by its vertical translocation/rotation. Accordingly, in vascular Kir6.1 channels, a greater energy barrier is involved in rotating the CD upward to interact with $PIP_2$ than in pancreatic channels whose Kir6.2-CD is more stably tethered to the membrane. This explains why Kir6.2-containing pancreatic channels are spontaneously active, while Kir6.1-containing vascular channels are not. By extension, vascular channel activation by Mg-nucleotides likely involves SUR2B-controlled upward movement of the Kir6.1-CD. It has been shown that Kir6.1 binds $PIP_2$ with higher affinity than Kir6.2 in biochemical assays and that once activated by Mg-nucleotides, vascular $K_{ATP}$ channels are highly stable and more resistant to $PIP_2$ depletion by polylysine than pancreatic channels (32). In our Kir6.1 structure, the Kir6.1-R70 sidechain is directed toward the lipid density in the $PIP_2$ binding pocket (Fig. 2*E*). Interestingly, in Kir6.2 the corresponding residue is a proline (P69). It is possible that this sequence variation may contribute to the higher $PIP_2$ affinity and stability of open vascular channels, but future studies are necessary to investigate this. Higher-$PIP_2$ affinity also accounts for long-standing results showing activated vascular $K_{ATP}$ channels are much less sensitive to ATP inhibition, as increased $PIP_2$ interaction reduces ATP inhibition in $K_{ATP}$ channels (16).

**SUR2B Dynamics.** Focused 3D classification resolved four distinct conformations, P1, P2, Q1, and Q2, showing variable SUR2B orientations (*SI Appendix*, Fig. S5 and Movie S1). P conformations differed from Q conformations by a large rotation of the ABC core of SUR2B relative to the Kir6.1 tetramer (~41° between P1 and Q1, about the axis defined by N447 in TMD1 and N69 in TMD0, respectively, compared to 63° rotational difference between the propeller and quatrefoil conformations in human pancreatic NBD-dimerized channels measured from the equivalent residues). Within P and Q, P1 and Q1 particles predominated over P2 and Q2. Transitions from P1 to P2 and Q1 to Q2 involved alternative rotation stops: P1's ABC core was 10° further away from Kir6.1 than P2's, while Q1's ABC core was 8° closer to Kir6.1 than in Q2. In short, Q1 was the tightest quatrefoil and P1 the most extended propeller. 3D variability analysis in CryoSPARC (*SI Appendix*, Fig. S6*a*) indicated SUR2B subunits moved independently between P- and Q-like positions (Movie S2). Further multibody refinement in RELION3 revealed greater heterogeneity within Q1 conformations than in P1, indicating wider dynamic range (*SI Appendix*, Fig. S6*b* and Movie S3).

Accompanying rotation, the SUR2B-ABC core also tilts away from Kir6.1. Tilting elevated the ABC core TMD in the Q conformations relative to P conformations (by 2.6 Å from P1 to Q1, measured at SUR2B-Y370; *SI Appendix*, Fig. S5*b*). Between the pancreatic $K_{ATP}$ propeller and quatrefoil forms (NBDs dimerized), the entire ABC-TMDs elevate ~3 Å without tilting (27). Tilt in our Q conformations may represent a partial transposition to be completed upon NBD dimerization. In the NBDs-dimerized pancreatic $K_{ATP}$, quatrefoil is the dominant class. Here, Q conformations were less common than P conformations among vascular $K_{ATP}$ channel structures in which the NBDs remain separated (*SI Appendix*, Fig. S2 and Table S1). Probabilities of SUR adopting P- or Q-like conformations therefore correlate with NBD dimerization state, although both occur regardless.

Rotation of SUR2B between P to Q conformations incorporated significant local structural changes. Extracellular contacts between transmembrane bundle 1 (TMB1) and TMD0 restructured both protein–protein and protein–lipid interactions (*SI Appendix*, Fig. S7). Hydrophobic and electrostatic interactions in P1 are lost in Q1, including T338, L339, and F344 in the TM6-TM7 loop of TMB1, with L165 and R166 in TM5 of TMD0. Moreover, a phosphatidylethanolamine molecule moved from between TM2 and TM7 in P1 to between TM3 and TM16 in Q1, likely stabilizing TMD0 and TMB1 interactions. Also noteworthy, in the pancreatic channel structure, SUR1 has an additional hydrophobic sequence ($^{340}$FLGVYFV$^{346}$), which anchors the TM6-TM7 loop to TMD0 (*SI Appendix*, Fig. S7*d* (23, 34). Absence of this sequence in SUR2B may impart flexibility that enables SUR2B to swing into Q conformations not observed in SUR1 when ATP and Glib are bound.

**The SUR2B-L0 Linker and the Glib Binding Pocket.** Transition between P and Q conformations remodeled cytoplasmic structural elements including L0, the N1-T2 linker, and Kir6.1 N-terminus (Kir6.1Nt), unexpectedly affecting interactions between SUR2B and Kir6.1. In SURx, L0 connects TMD0 to the ABC core and is crucial to $K_{ATP}$ gating (42–45). In SUR2B, we obtained two distinct L0 conformations, corresponding to P and Q conformers. In SUR2B-P1, we observed continuous cryoEM density of L0 (Fig. 3*A*). The well-defined N-terminal portion lacked secondary structure. The central portion formed an amphipathic helix, inserted between TMD0 and TMB1. A C-terminal helix then extended along the periphery of TMB1, paralleling the membrane. In contrast, L0 of SUR2B-Q1 comprised a destabilized N-terminal portion in which aa 197 to 213 were unresolved; a central amphipathic helix shifted into the cytoplasm, and a C-terminal helix pulled away from the Kir6.1 core (Fig. 3 and Movie S4). In addition, lipids around the amphipathic L0 helix in P1 conformation were replaced by the descended amphipathic helix in Q1 (Fig. 3*A*). Together, restructuring resulted in a marked decrease in contact area between SUR2B's TMD0 (M1-R256, including lipids) and the adjacent ABC core (A257-V1541 in P1; A257-A1543 in Q1), from 2,106.2 $\text{Å}^2$ in P1 to 1,208.0 $\text{Å}^2$ in Q1, which lowered the estimated free energy of formation at this interface from −43.0 kcal/mol in P1 to −18.4 kcal/mol in Q1 [calculated using Protein Data Bank in Europe (Proteins, Interfaces, Structures and Assemblies), abbreviated as PDBePISA (46)]. As noted, the P1 conformer predominates among the ATP- and Glib-bound vascular $K_{ATP}$ particles we observed. The simplest interpretation is that this interface is a principal determinant in maintaining SUR2B in P1 to a greater extent than Q1. The Q conformers would thus represent a divergent state in which a principal interface stabilizing a closed channel is compromised. It is worth noting that L0 in SUR1 (aa 192 to 262) is unresolved in the quatrefoil structure for the human pancreatic $K_{ATP}$ channel, in which NBDs are dimerized (PDB: 6C3O) (27). Therefore, the Q-like structures presented here may represent intermediary states that offer a glimpse into the conformational transitions of L0 that anticipate NBDs dimerization. The striking rearrangement of L0 likely results from the torque generated by rotation of the ABC core and further permits the channel to undergo the conformational changes for gating.

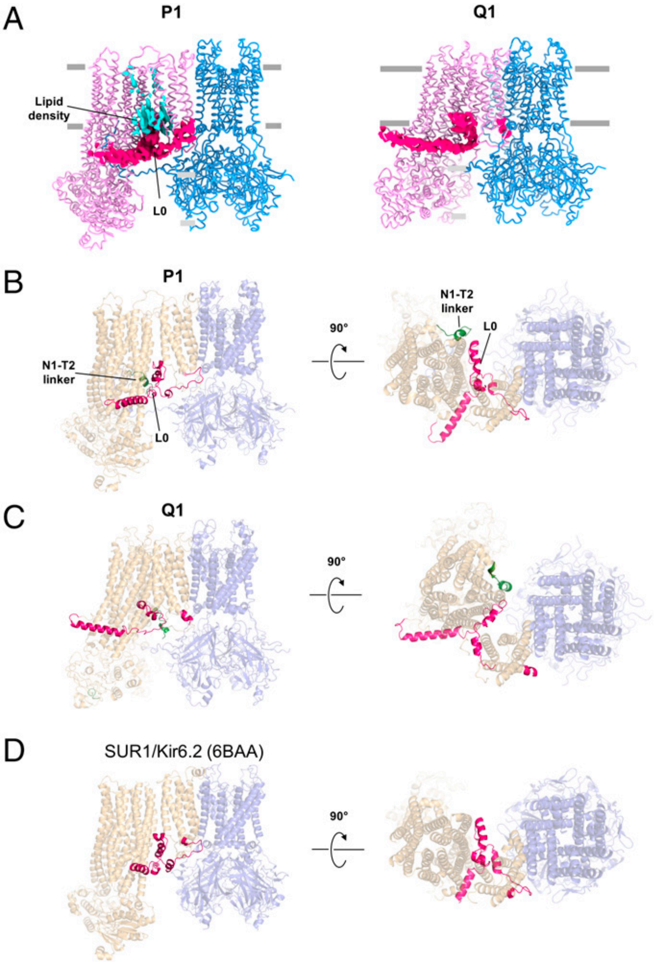

**Fig. 3.** SUR2B-L0 undergoes structural remodeling from P1 to Q1 conformations. (*A*) Comparison of the L0 cryoEM density (hot pink) in P1 and Q1 conformations. Lipid density seen in P1 but absent in Q1 is shown in cyan. (*B*) Structure of $(\text{Kir6.1})_4$SUR2B in P1 conformation showing L0 (red) viewed from the side (*Left*) and from the cytoplasmic side near the membrane (*Right*). The N1-T2 linker visible in these views is shown in green. (*C*) Structure of $(\text{Kir6.1})_4$SUR2B in Q1 conformation viewed from the side and the cytoplasm. (*D*) Structure of $(\text{Kir6.2})_4$SUR1 (PDB: 6BAA) bound to Glib and ATP for comparison.

Vascular $K_{ATP}$ channels are inhibited by Glib but are ∼10- to 50-fold less sensitive than pancreatic $K_{ATP}$ channels (17, 47). Glib cryoEM density was well resolved in both P1 and Q1 conformations of the vascular $K_{ATP}$ structure, where it bound within the same pocket of SUR2B (Fig. 4) as in SUR1 (24, 26). Also similar to pancreatic Kir6.2/SUR1 channels, cryoEM density of the distal KNt of Kir6.1 lay within the cleft between the two halves of the ABC core and immediately adjacent the Glib binding pocket (26). The structure model of the Glib binding site in P1 shows key interactions are largely conserved between SUR1 and SUR2B (Fig. 4*C*). However, the binding pose of Glib in the Q1 conformation is compressed compared to that in P1, with the Y1205 sidechain moved upward, which requires the 1-chloro-4-methoxy-benzene group to also move to avoid W423 in a neighboring helix (Fig. 4*C*). Also, an electrostatic interaction between chloride in Glib and nitrogen of R304 is eliminated in Q1. Worth noting, the SUR2B-Y1205 equivalent residue in SUR1 is S1238, and substitution of serine by tyrosine at this position has been shown to partly underlie Glib's lower-affinity inhibition of SUR2 channels (48). Of particular interest, substitution of S1238 to Y in SUR1 converts the Glib inhibition of pancreatic Kir6.2/SUR1 channels from nearly irreversible to readily reversible similar to SUR2-containing channels (49, 50), suggesting the S1238Y mutation may affect Glib off rate. This may arise through steric hindrance from the flexible tyrosine sidechain, as observed in the Q1 conformation.

The P1 to Q1 translocation was accompanied by more substantial change to the opposite side of the Glib binding pocket at F215, T227, and Y228 of the L0 linker (Fig. 4*C*). Previous studies of L0 of SUR1 have shown that Glib binding indirectly involves Y230 and W232 (Y228 and W230 in SUR2B), which stabilize the TM helices lining the Glib binding pocket (22); mutation of these residues to alanine reduces sensitivity to Glib (49, 50). In SUR2B P1 conformation, we found the hydrophobic Y228 and W230 sidechains, as well as F215 in the lower part of L0, similarly stabilized the TM helices along the Glib binding pocket (Fig. 4*C*), as occurs in SUR1. Specifically, F215 lay buried in a hydrophobic cavity formed by W230 from L0 and Y371, F1207, and L1206 from TMB1. However, in Q1, L0 was significantly remodeled at the interface with TMB1. In particular, a loop segment including P218-Y228 seen in P1 is raised and transformed into a helix in Q1. This helical element newly filled the hydrophobic cavity between TMD0 and TMB1, otherwise occupied by lipids in P1 (Fig. 3*A*). As further consequence in Q1, Y228 and F215 in L0 are displaced from the cavity, and Y371 and T227 occupy the space vacated by the sidechain of Y228. The movement of Y228 out of the cavity eliminates hydrophobic packing between L0 and the TM helices lining the Glib binding pocket, thus disrupting the integrity of the pocket

https://doi.org/10.1073/pnas.2109441118

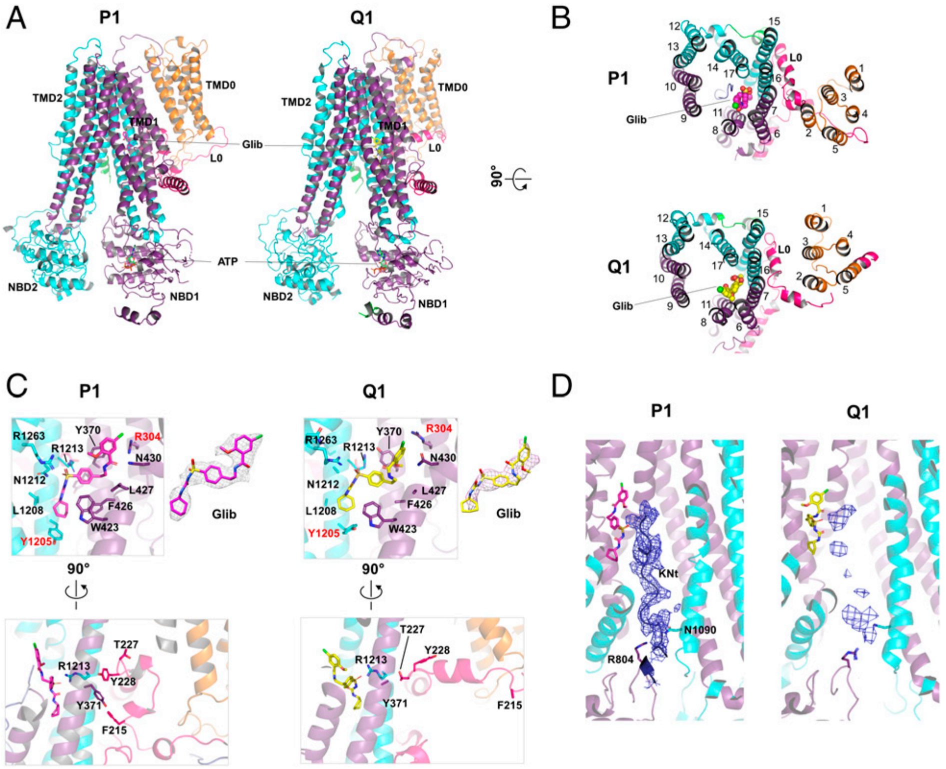

Fig. 4. Comparison of the SUR2B Glib binding pocket in P1 and Q1 conformations. (*A* and *B*) Overview from the side and the top, respectively. (*C*) Close-up view of the Glib binding site in P1 and Q1 conformations. Note the slightly different pose of Glib. Two key residues different in SUR2B and SUR1 are highlighted in red (R304 and Y1205). CryoEM density with the Glib structure model fitted into it is shown to the right of the binding site figure. *Bottom*: a different view of the Glib binding site highlighting the changes in L0 residues that impact the Glib binding site. (*D*) CryoEM density of the KNt in P1 and Q1 conformations. The KNt cryoEM density is stronger in P1 and allows modeling with a polyalanine chain. Note two residues in the NBD1 (R804) and TMD2 (N1090) sandwich the KNt to stabilize it in the central cavity between the two TMBs of SUR2B.

in similar fashion to the Y230A mutational effect in SUR1 (51). Lastly, the density of Kir6.1Nt in the ABC core central cleft also differed between P1 and Q1 (Fig. 4*D*). In P1, a strong continuous density of KNt was present, braced by R804 and N1090 of SUR2B, a pair of residues guarding entry to the cleft. The KNt density in Q1 was considerably weaker and discontinuous, indicating a more-labile conformation that may contribute to weak Glib binding at its adjacent pocket (26, 52). In summary, as the SUR2B-ABC core changes from P conformation to Q, L0 and Kir6.1Nt undergo remodeling that affects the Glib binding pocket.

**The N1-T2 Linker.** In all published pancreatic $K_{ATP}$ channel structures, the critical N1-T2 linker of SUR1 has remained unresolved (22–24, 26, 27, 34, 53), suggesting dynamic instability. In the density map of our vascular Kir6.1/SUR2B channel from the P1 particle set, the C-terminal end of the N1-T2 linker was sufficiently resolved (Fig. 5*A*), and we were able to build a polyalanine helical structure into the density map (residues 961 to 976). Density for the rest of N1-T2 (residues 911 to 960) remained largely unresolved in P1. However, the density for the entire linker was apparent in the map for our vascular $K_{ATP}$ channel Q1 structure (Fig. 5*B*), although resolution of residues 911 to 960 was insufficient for modeling. Specifically, the linker extended from NBD1 through the space between the two NBDs, then continued through the gap between the outer surface of NBD2 and the adjacent CTD of Kir6.1, before connecting to TMD2 (Fig. 5*B* and *SI Appendix*, Fig. S8). The location of the SUR2B N1-T2 linker contrasts sharply with locations of corresponding linkers in other ABCC proteins, including the Cl$^-$ channel CFTR and the yeast cadmium transporter Ycf1p. In CFTR, the N1-T2 linker equivalent is known as the R domain, which is phosphorylated by PKA to allow CFTR gating by Mg-nucleotides. In the unphosphorylated CFTR structure, the R domain is wedged in the cleft between the two halves of the ABC core, preventing NBD dimerization (54). In the phosphorylated CFTR structure, the R domain relocates to the outer surface of NBD1 (*SI Appendix*, Fig. S8), which allows NBD dimerization, hence CFTR gating by Mg-nucleotides (55, 56). In the Ycf1p structure, the N1-T2 linker is found at the outer surface of NBD1 similar to phosphorylated CFTR (57) even though the NBDs are separate. The peculiar location of the SUR2B N1-T2 linker suggests the linker has adopted a separate role in regulating functional coupling between SUR2B and Kir6.1.

In SUR2, the N1-T2 linker includes at its C-terminal end a stretch of 15 aa consisting exclusively of negative-charged glutamate and aspartate designated the ED-domain (947 to 961) (*SI Appendix*, Fig. S8), which is unique among all ABCC proteins. Previous mutational studies have implicated the ED-domain in transducing MgADP binding in SUR2A to opening of Kir6.2 (25). Disruption of the ED-domain prevented the normal activation response to MgADP and to pinacidil, a potassium channel opener. In the Q1 structure, the density corresponding to the ED-domain is sandwiched between NBD2 and Kir6.1-CTD (Fig. 5) and surrounded by positively charged residues from Kir6.1Nt, Kir6.1-CTD, and NBD2 of SUR2B (Fig. 5*B*), an array of partners for electrostatic interactions. To understand the potential molecular interactions and their functional relevance, we employed MD simulations of the (Kir6.1)$_4$SUR2B Q1 structure.

**MD Simulations Reveal MgADP-Dependent Dynamic Interactions between the ED-Domain, NBD2, and Kir6.1-CTD.** To assess conformational dynamics of the ED-domain and its interacting

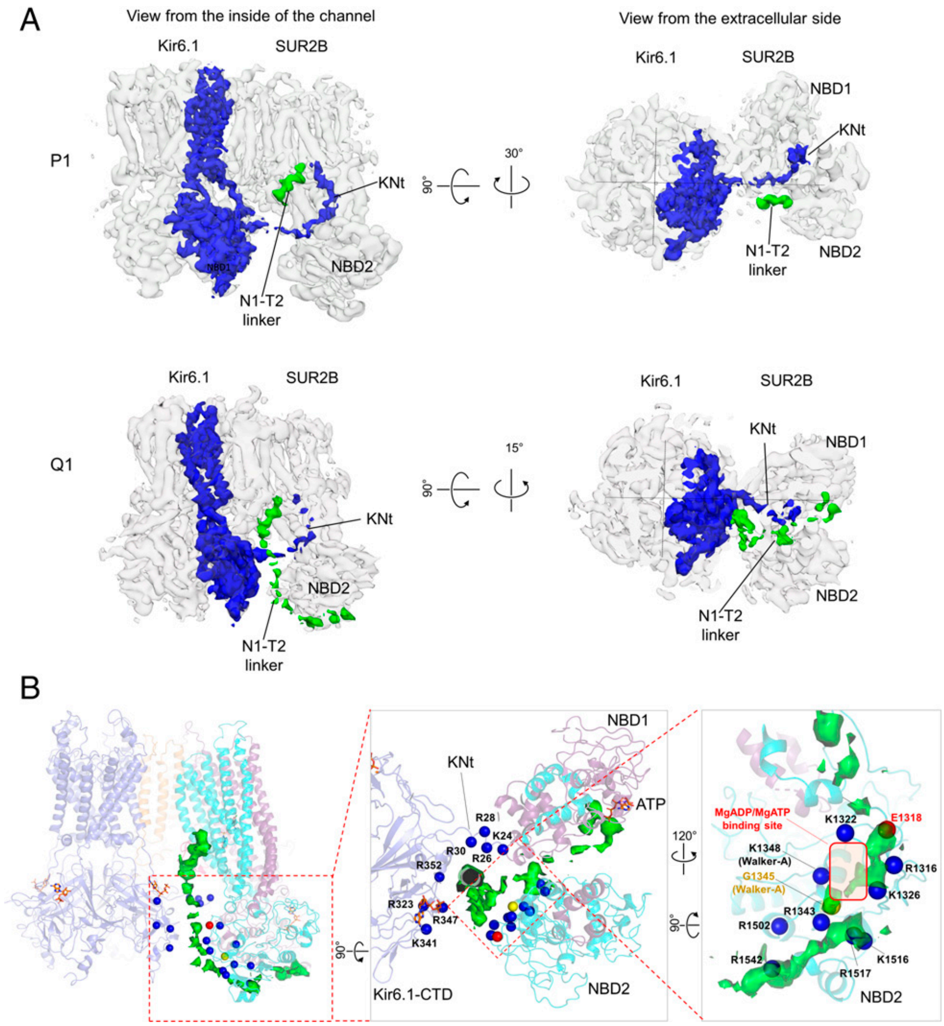

Fig. 5. Comparison of cryoEM densities of Kir6.1 N terminus and SUR2B N1-T2 linker in P1 and Q1 conformations. (*A*) Overall cryoEM density of (Kir6.1)$_4$-SUR2B in gray with density of one Kir6.1 and its N terminus (KNt) highlighted in blue and density of the SUR2B N1-T2 linker highlighted in green. (*B*) Close-up view of the N1-T2 linker density in (Kir6.1)$_4$SUR2B structure. Blue spheres are positively charged residues near the ED-domain. G1345 in the NBD2 Walker A motif and E1318 in the A-loop of NBD2 ($^{1315}$VRYEN$^{1319}$) are shown as reference points.

partners and how they may be dependent on the nucleotide binding status at the two NBDs, we performed simulations under two conditions. In one, ATP is bound to Kir6.1 and NBD1 of SUR2B, as present in our cryoEM structure. In the second condition, $Mg^{2+}$ is included with ATP bound at NBD1, and MgADP is docked into NBD2 (Fig. 6*A*). In both conditions, Glib was omitted from the structure to allow the SUR2B TMDs to be free of constraint during simulations. To assess reliability, three independent 1-µs simulations for each condition were carried out (*SI Appendix*, Fig. S9*a*). As with many biomolecular simulations, ours do not exhibit true equilibrium-like repeated fluctuations about mean values (58), although the combined 6 µs permitted structural inferences (Fig. 6 *C* and *E*). The root-mean-square fluctuation (RMSF) analyses showed high degrees of fluctuations of NBD1, the N1-T2 linker, and NBD2 (*SI Appendix*, Fig. S9*b*), consistent with overall lower resolutions of these domains in cryoEM maps (*SI Appendix*, Fig. S3*b*). However, particular interactions between the ED-domain and NBD2 depended on whether NBD2 was occupied by MgADP, and in turn those ED-domain–NBD2 interactions controlled direct interaction of NBD2 with Kir6.1-CTD.

During simulations, the ED-domain exchanged interactions between surrounding positively charged residues from Kir6.1Nt, Kir6.1-CTD, and NBD2 (Fig. 5*B* and Movies S5 and S6). When MgADP was absent at NBD2, the first one-half of the ED-domain (947 to 953) was most frequently in contact with SUR2B-NBD2 Walker A K1348; this was infrequent with MgADP bound at NBD2. To quantify MgADP dependence of the ED-domain–Walker A interaction, we measured the minimum distances between the ED-domain residues 947 to 953 and K1348 throughout simulations, comparing results with and without MgADP at NBD2 (Fig. 6 *B* and *C*). In the absence of MgADP, sidechain oxygens from ED residues were frequently within 4 Å of the sidechain nitrogen of K1348, supporting a salt bridge or strong electrostatic interaction (59). In contrast, in the presence of MgADP, ED residues remained too distant from K1348 for direct bonding. Moreover, in one MgADP simulation run in which MgADP dissociated (Fig. 6*C* red trace, ∼300 ns), the ED-domain subsequently moved to within 4 Å of K1348, the distance frequently observed in simulations lacking MgADP (Fig. 6*C*). The difference in ED–K1348 interactions between simulations is similarly evidenced by tracking the center of mass for C-α of ED residues 947 to 953 and the C-α of K1348 (Fig. 6*D*).

NBD2 also frequently formed close contacts with Kir6.1-CTD in the absence of MgADP but not when NBD2 included MgADP (Movies S5 and S6). With no MgADP, a loop

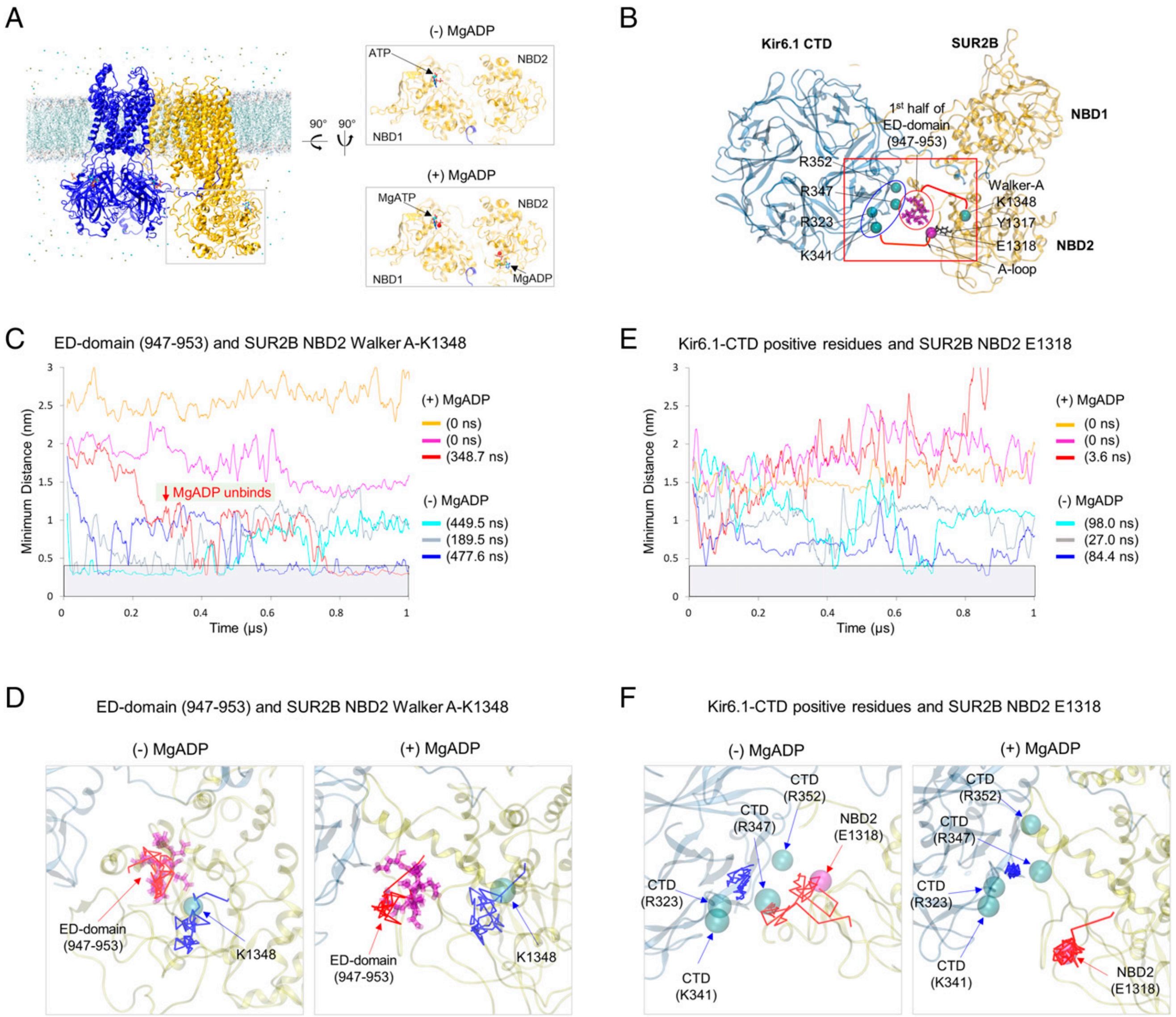

**Fig. 6.** MD simulations of the ED-domain dynamics in relation to SUR2B-NBD2 and Kir6.1-CTD. (*A*) MD simulation starting model (Q1) and conditions. In (−)MgADP condition, only ATP is present in NBD1. In (+)MgADP condition, MgADP is bound in NBD2 and MgATP is bound in NBD1. (*B*) Structural model marking residues of interest for distance analysis during MD simulations. These include the ED-domain residues (magenta sticks in red oval) and the Walker A K1348 (cyan sphere) in SUR2B NBD2 and R323, K341, R347, and R369 (cyan spheres in blue oval) in Kir6.1 CTD and E1318 in SUR2B NBD2. The A-loop containing Y1317, which coordinates adenine ring binding of MgADP is also labeled. (*C*) Measurement of minimum distance between the sidechain oxygen of any of the ED-domain 947 to 953 glutamate/aspartate residues and the sidechain nitrogen of K1348 in the three individual runs under both conditions. Note in one of the (+)MgADP runs (red), MgADP unbinds from NBD2 (marked by the red downward arrow). The gray bar marks the area where the distance is $\leq$4 Å. The total dwell time in distance $\leq$4 Å for each run is shown on the *Right*. Note the plot was window averaged with 10-ns scale, and the dwell time was calculated with raw data which has 100-ps scale (the same applies to *E*). (*D*) Movement of the center of mass of the C-$\alpha$ of the ED-domain residues 947 to 953 during simulation (red trace) relative to that of K1348 (blue trace). (*E*) Same as *C*, except the distance measured is between sidechain nitrogen of Kir6.1-CTD residues R323, K341, R347, R352, and the sidechain oxygen of E1318. (*F*) Same as *D*, except the blue trace represents the center of mass of the C-$\alpha$ of Kir6.1 CTD residues R323, K341, R347, R352, and the red trace is the C-$\alpha$ of E1318.

upstream of the Walker A motif in NBD2 ($^{1315}$VRYEN$^{1319}$, named A-loop for aromatic residue interacting with the adenine ring of ATP) (60) frequently extended across the intersubunit gap to interact with a cluster of positively charged residues in Kir6.1-CTD, including R323, K341, R347, and R352 (Movie S5). In direct contrast, when MgADP was bound to SUR2B-NBD2, the A-loop instead consistently interacted with MgADP at NBD2, far from the Kir6.1-CTD. The A-loop in SUR2B includes Y1317, which interacts with the adenine ring of bound MgADP at NBD2. Simultaneously, the dissociation of the ED-domain from Walker A K1348 that occurred with MgADP binding at NBD2 freed the ED-domain to move in between NBD2 and Kir6.1-CTD. There, the ED-domain interacted with positive-charged residues in Kir6.1-CTD that in the absence of MgADP interacted with NBD2 A-loop E1328 (Movies S5 and S6). Effectively, the Kir6.1-CTD exchanged the A-loop for the ED-domain and stabilized each conformation. Quantitatively, minimum distances measured between E1318 in A-loop and the four positive residues in Kir6.1-CTD documented the closer relation of A-loop and Kir6.1-CTD throughout the simulations in the absence of MgADP than when MgADP was bound (Fig. 6*E*). Minimum distance below 4 Å sufficient for E1318 salt bridge formation was seen in all three runs lacking MgADP but only transiently (3.6 ns) in a single of the three runs with MgADP (Fig. 6*E*). The nucleotide-dependent dynamics between the NBD2 A-loop and Kir6.1-CTD was also shown by tracking distance between the C-α of E1318 and center of the mass of the C-α for the Kir6.1-CTD–positive residues (an example run for each condition shown in Fig. 6*F*).

The dynamic, tripartite interactions between the ED-domain, NBD2, and Kir6.1-CTD, and the dependence of these interactions on MgADP found in MD simulations significantly advances our understanding of the mechanism of SUR-mediated channel stimulation by Mg-nucleotides. In the absence of MgADP, the ED-domain has preferred interactions with NBD2 Walker A K1348, while the A-loop E1318 is engaged with Kir6.1-CTD. This hinders NBD2 from undergoing further conformational transition toward that of the NBDs-dimerized human pancreatic channel quatrefoil structure (27), which shows SUR1-NBD2 further rotated toward NBD1 and also away from the positively charged residues in Kir6-CTD (PDB: 6C3O) (27). Upon MgADP binding to NBD2, the ED-domain is dissociated from K1348, while the NBD2 A-loop becomes stabilized by the bound MgADP, unable to extend toward Kir6.1-CTD. As a sequence of results, the ED-domain is free to move toward other surrounding positively charged residues including those in Kir6.1-CTD, which further prevents the interactions between NBD2 and Kir6.1-CTD, thus allowing NBD2 to undergo further rotation toward dimerization with NBD1. Supporting this understanding, an ion pair formed by R347 in the Kir6.1-CTD, with E1318 in the A-loop of SUR2B-NBD2, has previously been reported to play a role in channel activation by MgADP and the potassium channel opener pinacidil (61). Disruption of this ion pair by charge neutralization enhances MgADP/pinacidil gating, while charge swap restored wild-type–like sensitivity to MgADP/pinacidil (61). Our findings support the hypothesis that in order for NBDs to dimerize, interactions between SUR-NBD2 and Kir6-CTD must dissolve. Accordingly, disruption of the Kir6.1 R347-SUR2B E1318 salt bridge facilitates MgADP/pinacidil stimulation, as breaking the salt bridge promotes nucleotide binding at NBD2 and allows the further NBD2 movement needed for NBD dimerization and channel activation. The ED-domain in particular, by interacting with Walker A K1348, acts essentially as a mobile autoinhibitory motif, akin to autoinhibition mechanisms in many kinases (62), that occludes NBDs dimerization in the absence of MgADP and is deflected to permit dimerization

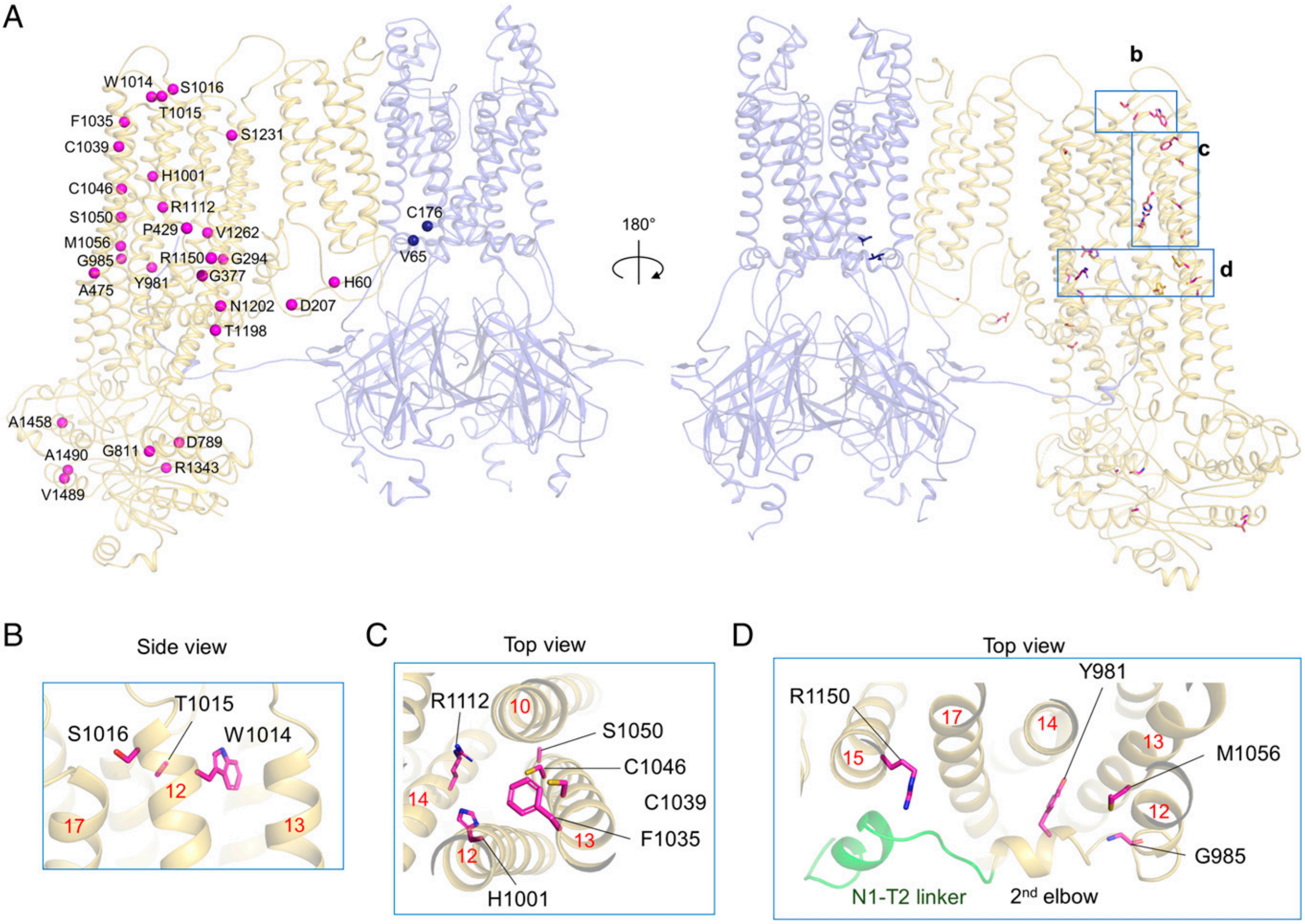

**Fig. 7.** Residues mutated in Cantú patients mapped onto the Kir6.1/SUR2B channel structure. (*A*) Residues mutated are shown as blue (Kir6.1) or magenta (SUR2B) in P1 conformation as spheres (*Left*) or in stick model (*Right*). Rat SUR2B numbering is used. Corresponding human mutations with rat residue in parentheses are as follows: H60Y (H60), D207E (D207), G294E (G294), G380C (G377), P432L (P429), A478V (A475), D793V (D789), G815A (G811), Y985S (Y981), G989E (G985), H1005L (H1001), W1018G (W1014), T1019E/K (T1015), S1020P (S1016), F1039S (F1035), S1054Y (S1050), C1043Y (C1039), C1050F (C1046), M1060I (M1056), R1116H/C/G (R1112), R1154G/Q/W (R1150), T1202M (T1198), N1206K (N1202), S1235F (S1231), V1266M (V1262), R1347C (R1343), A1462G (A1458), V1490E (V1489), and A1494T (A1490). (*B*–*D*) Close-up side or top views of boxed regions labeled in the overall structure in *A* (*Right*). In *D*, the N1-T2 linker is colored green and labeled together with the second elbow helix leading to TM12 of TMD2 in SUR2B. Red numbers mark the TM helices shown.

when MgADP has bound to NBD2. In this way, the ED-domain functions as a gatekeeper to prevent unregulated channel activation in the absence of MgADP.

**Implications for Cantú Mutations.** Taken together, our structures and MD simulations capture conformations that appear intermediate between the NBD-separated inactive and NBD-dimerized active states. The structural knowledge sheds light on how Cantú mutations (Fig. 7*A*) may cause gain of function in vascular $K_{ATP}$ channels. In Kir6.1, V65M in the SH and C176S in the pore-lining helix likely enhance function by increasing channel $P_o$, which has been demonstrated in equivalent mutations in Kir6.2 (63). Most Cantú mutations identified to date are in *ABCC9*. Significantly, many of them affect residues in TM12, including Y981 and G985 in the second elbow helix, and W1014, T1015, and S1016 at the top (Fig. 7). TM12 is connected to the N1-T2 linker (Fig. 7*D*). Many other Cantú mutations are in domains interacting with TM12, including a series throughout TM13 (F1035, C1039, C1046, S1050, and M1056), as well as H1001 in TM12 and R1112 in TM14, which interface TM13 (Fig. 7*C*). One most frequently mutated residue R1150 of TM15 is adjacent to the structured helix portion of the N1-T2 linker, C-terminal to the ED-domain (Fig. 7*D*). The interconnectivity of these residues and their association with the N1-T2 linker suggest they may in common govern a critical conformational change during channel gating by Mg-nucleotides at the NBDs. Consistent with this notion, Y981S, G985E, and M1056I have been shown to enhance channel response to MgADP stimulation (42). Of note, C1039Y in TM13, has been shown to increase channel $P_o$ similar to D207E in L0, rather than enhance MgADP response (42). It is possible that C1039Y alters interactions of SUR-TMDs with Kir6.1Nt and/or Kir6.1-TMs to affect channel $P_o$. Finally, two other mutations that also enhance MgADP response but are not directly connected to the N1-T2 linker are P429L in TM8 and A475V in TM9 of TMD1 (42). TM8 and TM9 are part of the TM bundles above NBD1 and NBD2 respectively, and P429L and A475V may affect the dynamics of the NBDs to alter MgADP response. Future studies correlating the effects of Cantú mutations on channel conformations and gating will further illuminate the structural basis of channel gating and in turn mechanisms of disease mutations.

**Summary.** Insights into how a particular complex operates is often gained by comparing related complexes, anticipating that similarities and differences in structure and function will correlate. In this study, we sought to determine the cryoEM structure of vascular $K_{ATP}$ channels, composed of Kir6.1 and SUR2B, in the presence of ATP and Glib, for comparison to pancreatic $K_{ATP}$ channel (Kir6.2/SUR1) structures determined with the same conditions. The structures we obtained reveal multiple elements showing distinct configurations that may account for channel-specific conductance, ATP inhibition, and drug sensitivities. In contrast, the serendipitous appearance of quatrefoil-like conformations, and SURx linkers which have been missing in previous $K_{ATP}$ structures and are now seen at critical domain interfaces, affords insights into the long-sought structural dynamics shared by $K_{ATP}$ channels in regulating their activity. The Q conformations adopted by SUR2B are most simply interpreted as transitional states between the inactive NBD-separated and the active NBD-dimerized SUR conformations.

The several conformations isolated from the cryoEM dataset, together with the dynamics revealed by 3D variability analyses and captured by MD simulations, suggest a model hypothesis for how Mg-nucleotide interactions with SUR2B activates Kir6.1 (Fig. 8). In this model, individual SUR2B subunits transition between P and Q conformations. In the Q conformations and without Mg-nucleotides at NBD2, the ED-domain in the N1-T2 linker acts as an autoinhibitory motif that prevents unregulated activation. Specifically, ED-domain interaction with Walker A K1348 at NBD2 promotes electrostatic interaction between NBD2 A-loop and Kir6.1-CTD, which further corrupts the Mg-nucleotide binding site and

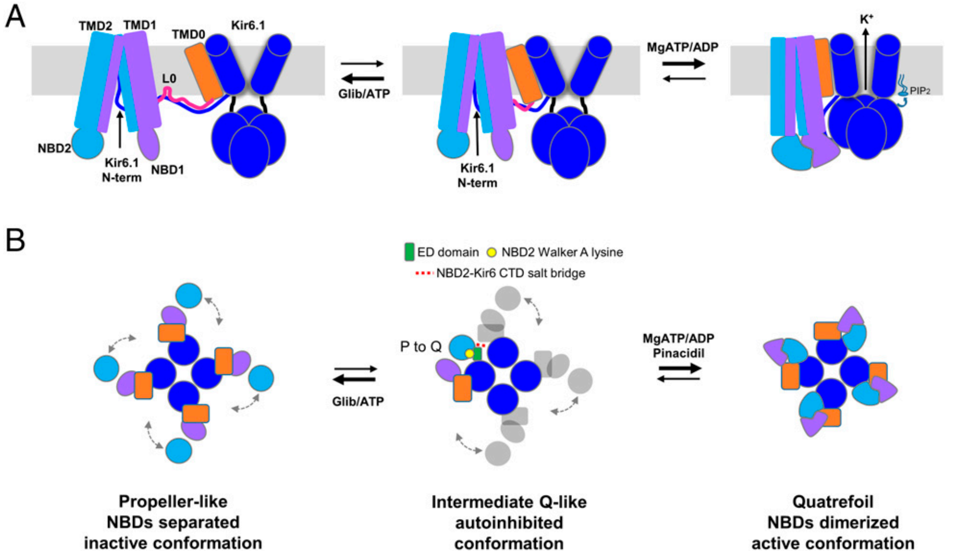

**Fig. 8.** Proposed model of vascular $K_{ATP}$ channel conformational dynamics. Cartoon representation of channel side view (*A*) and top/down view (*B*) in inactive P conformation, Q-like intermediate conformation (only one SUR2B is colored to highlight structural interactions), and active, NBD-dimerized quatrefoil conformation. In the presence of Glib and ATP, the P conformation dominates. Addition of MgATP/ADP promotes NBD dimerization, which is postulated to cause Kir6.1-CTD to move close to the membrane to interact with $PIP_2$ for channel opening. In *B*, individual SUR subunits undergo P-Q conformation transitions independently. In the absence of MgADP at NBD2, the ED-domain interacts with NBD2-Walker A lysine (1348). The A-loop E1318 in NBD2 forms salt bridges with positively charged residues in Kir6.1-CTD, preventing further rotation of NBD2 needed for NBDs dimerization, thus arresting SUR in an autoinhibited intermediate conformation. Increasing MgATP/ADP concentrations increases the probability of MgATP/ADP binding to all SUR2B subunits to release autoinhibition and promotes conformational change to the NBD-dimerized quatrefoil state for channel activation.

also withholds NBD2 from dimerization with NBD1. Addition of Mg-nucleotides relieves autoinhibition imposed by the ED-domain, coupling organization of the Mg-nucleotide binding site to liberation of NBD2 to rotate toward NBD1 for dimerization. Yet-to-be-determined mechanisms are required to explain how dimerization of NBDs in SUR2B leads Kir6.1-CTD to move up to the membrane to interact with $PIP_2$ for channel opening. The model would predict that inhibitory ligands such as Glib or stimulatory ligands such as Mg-nucleotides or the potassium channel opener pinacidil, are able to shift the equilibrium of SUR2B toward P or Q conformations to drive channel closure or opening, respectively. It is important to note that dimerization of the NBDs was not observed during the 1-μs simulation in the presence of MgADP/MgATP; moreover, only one SUR2B is present in the simulations, which prevents consideration of potential structural impact of neighboring SUR2B subunits. Future structures with NBDs dimerized and MD simulations of the full channel are required to confirm and extend our understanding of $K_{ATP}$ channel activation. This notwithstanding, we speculate the general scheme of the model applies to other $K_{ATP}$ channels with variations to explain isoform-specific sensitivities for Mg-nucleotides and drugs. The structures presented here serve as a framework for understanding channel regulation and dysregulation and will aid development of isoform-specific pharmacological modulators to correct channel defects in Cantú and other diseases involving vascular $K_{ATP}$ dysfunction.

## Materials and Methods

Expression and purification of Kir6.1/SUR2B channels, cryoEM imaging, data processing, and modeling were performed using published protocols (22, 23, 26, 64) and are described in detail in *SI Appendix*. Briefly, recombinant adenoviruses containing the coding sequences of Kir6.1 and FLAG-tagged SUR2B were used to infect COSm6 cells and expressed channels purified via the FLAG tag. Purified channel complexes were spotted on grids coated with graphene-oxide, vitrified, and imaged on a Titan Krios 300 kV cryoelectron microscope. Image processing and analysis were carried out in RELION-3.0 and CryoSPARC. Models were built by fitting previously published Kir6.2/SUR1 structures and in SWISS-MODEL and refined in Coot and Phenix.

MD simulations were performed at all-atom resolution using AMBER 16 (65) with graphics processing unit (GPU) acceleration. The starting structure was developed from the Q1 model (four Kir6.1 and one SUR2B) with flexible linkers built in SWISS-MODEL. Glib was removed to allow the TMDs to relax during simulations. The structures were protonated at pH 7 and inserted in a bilayer membrane composed of 1-palmitoyl-2-oleoyl-phosphatidylcholine lipids and surrounded by an aqueous solution of 0.15 M KCl. Pairwise distances were analyzed from the simulated trajectories using the gmx pairdist tool in Gromacs 2019.4 (66). Detailed methods for MD simulations and data analysis are provided in *SI Appendix*.

**Data Availability.** CryoEM density maps have been deposited to the Electron Microscopy Data Bank (P1: EMD-23864, P2: EMD-23881, Q1: EMD-23880, and Q2: EMD-23882). Coordinates for $(Kir6.1)_4SUR2B$ atomic models have been deposited to the Protein Data Bank (P1: 7MIT, P2: 7MJP, Q1: 7MJO, and Q2: 7MJQ). MD simulation data have been deposited to the open-access repository Zenodo (5546127). All other study data are included in the article and/or supporting information.

**ACKNOWLEDGMENTS.** A portion of this research was supported by NIH Grant No. U24GM129547 and performed at the Pacific Northwest Cryo-EM Center (PNCC) at Oregon Health and Science University (OHSU) and accessed through the Environmental Molecular Sciences Laboratory (EMSL) (grid.436923.9), a Department of Energy Office (DOE) of Science User Facility sponsored by the Office of Biological and Environmental Research. We also thank Dr. Nancy Meyer at the PNCC and staff at the Multiscale Microscopy Core of OHSU for technical support. We acknowledge the support by the NIH Grant No. R01DK066485 (to S.-L.S.) and by the NSF Grant No. MCB 17158233 (to D.M.Z.).

1. C. G. Nichols, KATP channels as molecular sensors of cellular metabolism. *Nature* **440**, 470–476 (2006).
2. L. Aguilar-Bryan *et al.*, Toward understanding the assembly and structure of KATP channels. *Physiol. Rev.* **78**, 227–245 (1998).
3. M. N. Foster, W. A. Coetzee, KATP channels in the cardiovascular system. *Physiol. Rev.* **96**, 177–252 (2016).
4. A. P. Babenko, L. Aguilar-Bryan, J. Bryan, A view of sur/KIR6.X, KATP channels. *Annu. Rev. Physiol.* **60**, 667–687 (1998).
5. M. T. Nelson, J. M. Quayle, Physiological roles and properties of potassium channels in arterial smooth muscle. *Am. J. Physiol.* **268**, C799–C822 (1995).
6. M. T. Nelson, J. B. Patlak, J. F. Worley, N. B. Standen, Calcium channels, potassium channels, and voltage dependence of arterial smooth muscle tone. *Am. J. Physiol.* **259**, C3–C18 (1990).
7. M. T. Nelson, N. B. Standen, J. E. Brayden, J. F. Worley, 3rd, Noradrenaline contracts arteries by activating voltage-dependent calcium channels. *Nature* **336**, 382–385 (1988).
8. Q. Aziz *et al.*, The ATP-sensitive potassium channel subunit, Kir6.1, in vascular smooth muscle plays a major role in blood pressure control. *Hypertension* **64**, 523–529 (2014).
9. Y. Huang, D. Hu, C. Huang, C. G. Nichols, Genetic discovery of ATP-sensitive $K^+$ channels in cardiovascular diseases. *Circ. Arrhythm. Electrophysiol.* **12**, e007322 (2019).
10. B. W. van Bon *et al.*, Cantú syndrome is caused by mutations in ABCC9. *Am. J. Hum. Genet.* **90**, 1094–1101 (2012).
11. M. Harakalova *et al.*, Dominant missense mutations in ABCC9 cause Cantú syndrome. *Nat. Genet.* **44**, 793–796 (2012).
12. D. K. Grange *et al.*, Cantú syndrome: Findings from 74 patients in the International Cantú Syndrome Registry. *Am. J. Med. Genet. C. Semin. Med. Genet.* **181**, 658–681 (2019).
13. F. M. Ashcroft, F. M. Gribble, Correlating structure and function in ATP-sensitive K+ channels. *Trends Neurosci.* **21**, 288–294 (1998).
14. T. Baukrowitz *et al.*, PIP2 and PIP as determinants for ATP inhibition of KATP channels. *Science* **282**, 1141–1144 (1998).
15. O. Fürst, B. Mondou, N. D'Avanzo, Phosphoinositide regulation of inward rectifier potassium (Kir) channels. *Front. Physiol.* **4**, 404 (2014).
16. S. L. Shyng, C. G. Nichols, Membrane phospholipid control of nucleotide sensitivity of KATP channels. *Science* **282**, 1138–1141 (1998).
17. A. Fujita, Y. Kurachi, Molecular aspects of ATP-sensitive K+ channels in the cardiovascular system and K+ channel openers. *Pharmacol. Ther.* **85**, 39–53 (2000).
18. W. W. Shi, Y. Yang, Y. Shi, C. Jiang, K(ATP) channel action in vascular tone regulation: From genetics to diseases. *Sheng Li Xue Bao* **64**, 1–13 (2012).
19. A. Tinker, Q. Aziz, Y. Li, M. Specterman, ATP-sensitive potassium channels and their physiological and pathophysiological roles. *Compr. Physiol.* **8**, 1463–1511 (2018).
20. C. McClenaghan *et al.*, Glibenclamide reverses cardiovascular abnormalities of Cantu syndrome driven by KATP channel overactivity. *J. Clin. Invest.* **130**, 1116–1121 (2020).
21. A. Ma *et al.*, Glibenclamide treatment in a Cantú syndrome patient with a pathogenic ABCC9 gain-of-function variant: Initial experience. *Am. J. Med. Genet. A.* **179**, 1585–1590 (2019).
22. G. M. Martin, B. Kandasamy, F. DiMaio, C. Yoshioka, S. L. Shyng, Anti-diabetic drug binding site in a mammalian $K_{ATP}$ channel revealed by Cryo-EM. *eLife* **6**, e31054 (2017).
23. G. M. Martin *et al.*, Cryo-EM structure of the ATP-sensitive potassium channel illuminates mechanisms of assembly and gating. *eLife* **6**, e24149 (2017).
24. J. X. Wu *et al.*, Ligand binding and conformational changes of SUR1 subunit in pancreatic ATP-sensitive potassium channels. *Protein Cell* **9**, 553–567 (2018).
25. A. B. Karger *et al.*, Role for SUR2A ED domain in allosteric coupling within the K(ATP) channel complex. *J. Gen. Physiol.* **131**, 185–196 (2008).
26. G. M. Martin *et al.*, Mechanism of pharmacochaperoning in a mammalian $K_{ATP}$ channel revealed by cryo-EM. *eLife* **8**, e46417 (2019).
27. K. P. K. Lee, J. Chen, R. MacKinnon, Molecular structure of human KATP in complex with ATP and ADP. *eLife* **6**, e32481 (2017).
28. Y. Zhao, Z. Chen, Z. Cao, W. Li, Y. Wu, Diverse structural features of potassium channels characterized by scorpion toxins as molecular probes. *Molecules* **24**, 2045 (2019).
29. V. P. Repunte *et al.*, Extracellular links in Kir subunits control the unitary conductance of SUR/Kir6.0 ion channels. *EMBO J.* **18**, 3317–3324 (1999).
30. J. Yang, M. Yu, Y. N. Jan, L. Y. Jan, Stabilization of ion selectivity filter by pore loop ion pairs in an inwardly rectifying potassium channel. *Proc. Natl. Acad. Sci. U.S.A.* **94**, 1568–1572 (1997).
31. R. S. Vieira-Pires, J. H. Morais-Cabral, 3(10) helices in channels and other membrane proteins. *J. Gen. Physiol.* **136**, 585–592 (2010).
32. K. V. Quinn, Y. Cui, J. P. Giblin, L. H. Clapp, A. Tinker, Do anionic phospholipids serve as cofactors or second messengers for the regulation of activity of cloned ATP-sensitive K+ channels? *Circ. Res.* **93**, 646–655 (2003).
33. A. L. Duncan, R. A. Corey, M. S. P. Sansom, Defining how multiple lipid species interact with inward rectifier potassium (Kir2) channels. *Proc. Natl. Acad. Sci. U.S.A.* **117**, 7803–7813 (2020).
34. D. Ding, M. Wang, J. X. Wu, Y. Kang, L. Chen, The structural basis for the binding of repaglinide to the pancreatic KATP channel. *Cell Rep.* **27**, 1848–1857.e4 (2019).
35. M. Yamada *et al.*, Sulphonylurea receptor 2B and Kir6.1 form a sulphonylurea-sensitive but ATP-insensitive K+ channel. *J. Physiol.* **499**, 715–720 (1997).

36. E. Satoh *et al.*, Intracellular nucleotide-mediated gating of SUR/Kir6.0 complex potassium channels expressed in a mammalian cell line and its modification by pinacidil. *J. Physiol.* **511**, 663–674 (1998).
37. S. B. Hansen, X. Tao, R. MacKinnon, Structural basis of PIP2 activation of the classical inward rectifier K+ channel Kir2.2. *Nature* **477**, 495–498 (2011).
38. M. R. Whorton, R. MacKinnon, Crystal structure of the mammalian GIRK2 K+ channel and gating regulation by G proteins, PIP2, and sodium. *Cell* **147**, 199–208 (2011).
39. V. N. Bavro *et al.*, Structure of a KirBac potassium channel with an open bundle crossing indicates a mechanism of channel gating. *Nat. Struct. Mol. Biol.* **19**, 158–163 (2012).
40. O. B. Clarke *et al.*, Domain reorientation and rotation of an intracellular assembly regulate conduction in Kir potassium channels. *Cell* **141**, 1018–1029 (2010).
41. Y. Niu, X. Tao, K. K. Touhara, R. MacKinnon, Cryo-EM analysis of $PIP_2$ regulation in mammalian GIRK channels. *eLife* **9**, e60552 (2020).
42. C. McClenaghan *et al.*, Cantu syndrome-associated SUR2 (ABCC9) mutations in distinct structural domains result in $K_{ATP}$ channel gain-of-function by differential mechanisms. *J. Biol. Chem.* **293**, 2041–2052 (2018).
43. T. Pipatpolkai, S. Usher, P. J. Stansfeld, F. M. Ashcroft, New insights into $K_{ATP}$ channel gene mutations and neonatal diabetes mellitus. *Nat. Rev. Endocrinol.* **16**, 378–393 (2020).
44. A. P. Babenko, J. Bryan, Sur domains that associate with and gate KATP pores define a novel gatekeeper. *J. Biol. Chem.* **278**, 41577–41580 (2003).
45. R. Masia *et al.*, A mutation in the TMD0-L0 region of sulfonylurea receptor-1 (L225P) causes permanent neonatal diabetes mellitus (PNDM). *Diabetes* **56**, 1357–1362 (2007).
46. E. Krissinel, K. Henrick, Inference of macromolecular assemblies from crystalline state. *J. Mol. Biol.* **372**, 774–797 (2007).
47. U. Russ, U. Lange, C. Löffler-Walz, A. Hambrock, U. Quast, Interaction of the sulfonylthiourea HMR 1833 with sulfonylurea receptors and recombinant ATP-sensitive K(+) channels: Comparison with glibenclamide. *J. Pharmacol. Exp. Ther.* **299**, 1049–1055 (2001).
48. R. Ashfield, F. M. Gribble, S. J. Ashcroft, F. M. Ashcroft, Identification of the high-affinity tolbutamide site on the SUR1 subunit of the K(ATP) channel. *Diabetes* **48**, 1341–1347 (1999).
49. F. F. Yan, J. Casey, S. L. Shyng, Sulfonylureas correct trafficking defects of disease-causing ATP-sensitive potassium channels by binding to the channel complex. *J. Biol. Chem.* **281**, 33403–33413 (2006).
50. P. K. Devaraneni, G. M. Martin, E. M. Olson, Q. Zhou, S. L. Shyng, Structurally distinct ligands rescue biogenesis defects of the KATP channel complex via a converging mechanism. *J. Biol. Chem.* **290**, 7980–7991 (2015).
51. W. H. Vila-Carriles, G. Zhao, J. Bryan, Defining a binding pocket for sulfonylureas in ATP-sensitive potassium channels. *FASEB J.* **21**, 18–25 (2007).
52. P. Kühner *et al.*, Importance of the Kir6.2 N-terminus for the interaction of glibenclamide and repaglinide with the pancreatic K(ATP) channel. *Naunyn Schmiedebergs Arch. Pharmacol.* **385**, 299–311 (2012).
53. N. Li *et al.*, Structure of a pancreatic ATP-sensitive potassium channel. *Cell* **168**, 101–110.e10 (2017).
54. F. Liu, Z. Zhang, L. Csanády, D. C. Gadsby, J. Chen, Molecular structure of the human CFTR ion channel. *Cell* **169**, 85–95.e8 (2017).
55. Z. Zhang, F. Liu, J. Chen, Conformational changes of CFTR upon phosphorylation and ATP binding. *Cell* **170**, 483–491.e8 (2017).
56. L. Csanády, P. Vergani, D. C. Gadsby, Structure, gating, and regulation of the Cftr anion channel. *Physiol. Rev.* **99**, 707–738 (2019).
57. S.C. Bickers, S. Benlekbir, J. L. Rubinstein, V. Kanelis, Structure of Ycf1p reveals the transmembrane domain TMD0 and the regulatory R region of ABCC transporters. *Proc. Natl. Acad. Sci. U.S.A.* **118**, e2025853118 (2021).
58. A. Grossfield *et al.*, Best practices for quantification of uncertainty and sampling quality in molecular simulations [Article v1.0]. *Living J. Comput. Mol. Sci.* **1**, 5067 (2018).
59. S. Kumar, R. Nussinov, Relationship between ion pair geometries and electrostatic strengths in proteins. *Biophys. J.* **83**, 1595–1612 (2002).
60. S. V. Ambudkar, I. W. Kim, D. Xia, Z. E. Sauna, The A-loop, a novel conserved aromatic acid subdomain upstream of the Walker A motif in ABC transporters, is critical for ATP binding. *FEBS Lett.* **580**, 1049–1055 (2006).
61. D. Lodwick *et al.*, Sulfonylurea receptors regulate the channel pore in ATP-sensitive potassium channels via an intersubunit salt bridge. *Biochem. J.* **464**, 343–354 (2014).
62. G. M. Cheetham, Novel protein kinases and molecular mechanisms of autoinhibition. *Curr. Opin. Struct. Biol.* **14**, 700–705 (2004).
63. P. E. Cooper, C. McClenaghan, X. Chen, A. Stary-Weinzinger, C. G. Nichols, Conserved functional consequences of disease-associated mutations in the slide helix of Kir6.1 and Kir6.2 subunits of the ATP-sensitive potassium channel. *J. Biol. Chem.* **292**, 17387–17398 (2017).
64. C. M. Driggers, S. L. Shyng, Production and purification of ATP-sensitive potassium channel particles for cryo-electron microscopy. *Methods Enzymol.* **653**, 121–150 (2021).
65. D. A. Case *et al.*, AMBER 2016. University of California, San Francisco. (2016). https://ambermd.org/doc12/Amber16.pdf. Accessed 11 October 2021.
66. M. J. Abraham *et al.*, GROMACS: High performance molecular simulations through multi-level parallelism from laptops to supercomputers. *SoftwareX* **1–2**, 19–25 (2015).